Ceramics International 43 (2017) 7851–7860

Contents lists available at ScienceDirect

Ceramics International

journal homepage: www.elsevier.com/locate/ceramint

Synthesis and characterization of mesoporous NiO_2/ZrO_2-CeO_2 catalysts for total methane conversion

R. Bacani[a], L.M. Toscani[b], T.S. Martins[c,*], M.C.A. Fantini[a], D.G. Lamas[d,e], S.A. Larrondo[b,f]

[a] Departamento de Física Aplicada, Instituto de Física, Universidade de São Paulo, Rua do Matão 1371, Cidade Universitária, 05508-090 São Paulo, Brazil
[b] UNIDEF, MINDEF, CONICET, Departamento de Investigaciones en Sólidos, CITEDEF, J.B. de La Salle 4397, 1603 Villa Martelli, Pcia. de Buenos Aires, Argentina
[c] Departamento de Ciências Exatas e da Terra, Instituto de Ciências Ambientais, Químicas e Farmacêuticas, Universidade Federal de São Paulo – UNIFESP, Rua São Nicolau 210, 2º andar, Diadema 09913-030, São Paulo, Brazil
[d] CONICET/Escuela de Ciencia y Tecnología, Universidad Nacional de General San Martín, Martín De Irigoyen 3100, Edificio Tornavía, Campus Miguelete, 1650 San Martín, Pcia. de Buenos Aires, Argentina
[e] Departamento de Física de la Materia Condensada, Gerencia de Investigación y Aplicaciones, Centro Atómico Constituyentes, Comisión Nacional de Energía Atómica, Av. General Paz 1499, 1650 San Martín, Pcia de Buenos Aires, Argentina
[f] Instituto de Investigación e Ingeniería Ambiental, Universidad Nacional de General San Martín, Campus Miguelete, 25 de Mayo y Francia, 1650 San Martín, Pcia. de Buenos Aires, Argentina

ARTICLE INFO

Keywords:
Ceria
Zirconia
Nickel
Anodes
SOFC
Methane oxidation

ABSTRACT

This work reports the synthesis and characterization of mesoporous NiO/ZrO_2-CeO_2 composites. These materials are still being developed due to their excellent morphological and structural properties, especially for solid oxide fuel cells (SOFCs) anodes. A soft chemical route using a polymeric template was utilized to synthesize the samples. The structure after two different calcination processes at 400 °C and 540 °C was studied by X-ray diffraction and Rietveld refinement, before and after NiO loading. Nitrogen adsorption, scanning/transmission electron microscopy and small angle X-ray scattering revealed a nanocrystalline bi-phasic porous material. Temperature programmed reduction experiments showed higher Ni and Ce reduction values for samples calcined at 400 °C and 540 °C, respectively. Methane conversion values in the temperature range studied were similar for both calcination temperatures, showing 50% CH_4 conversion around 550 °C and 80% around 650 °C. However, a sample calcined at 400 °C exhibited better morphological and textural properties leading to an enhancement in NiO and CeO_2 reducibility that might be responsible for an improvement in oxygen surface exchange and gasification of carbon species in catalytic experiments.

1. Introduction

Ceria-based materials are well known for excellent catalytic performance due to the cerium oxide redox/oxygen storage properties [1–6]. Specially, ceria-zirconia solid solutions are used in many catalytic and electrocatalytic applications such as automotive three-way catalysts (TWCs) [7], oxidation and reforming catalysts [5,8–14], electrode materials in solid oxide fuel cells (SOFCs) [15–17] and constitutive materials in electrocatalytic devices [18–20].

The synthesis of mesoporous (2 < pores sizes < 50 nm) ceria-zirconia materials via soft template methods is a useful strategy to produce these solids since they are more versatile and are conducted at lower temperature, compared to other synthesis procedures [6,12,21–25]. Several attempts to synthesize zirconia doped ceria (ZDC) with better textural/structural properties were reported in the last decades [8,26–28]. This material is a mixed ionic-electronic conductor (MIEC) under reducing atmosphere, which is an important feature for SOFC applications because the fuel oxidation reaction takes place over the entire anode surface of the material and not only in the triple phase boundary (TPB) as in the case of the electronic conductors [28]. The synthesis by the gel-combustion, citrate and freeze-drying methods provide materials with suitable properties for many applications [29–37]. Given the fact that the electronic conductivity of ZDC is relatively low, it is typically used in composites with a metal conductor. Nickel is the most common choice due to its lower cost and high catalytic activity for methane oxidation [11,35,36,38].

* Corresponding author. Current address: Federal University of São Paulo, Department of Exact and Earth Science, Rua São Nicolau, 210, 2nd floor, 09913-030 Diadema, São Paulo, Brazil.
E-mail addresses: rbacani@usp.br (R. Bacani), ltoscani@citedef.gob.ar (L.M. Toscani), tsmartins@unifesp.br (T.S. Martins), mfantini@if.usp.br (M.C.A. Fantini), diego.g.lamas@gmail.com (D.G. Lamas), slarrondo@unsam.edu.ar (S.A. Larrondo).

http://dx.doi.org/10.1016/j.ceramint.2017.03.101
Received 24 February 2017; Received in revised form 16 March 2017; Accepted 16 March 2017
Available online 18 March 2017

Ni/Yttria-stabilized zirconia (YSZ) anode is the most studied and tested in SOFCs, providing high power density values when operating at temperatures between 750 °C and 850 °C [39–41], using H_2 and CH_4 as the fuel source. It was found that the conversion rate of methane is strongly dependent on the specific surface area of the anode [41], indicating the importance to control the morphology of the anode in order to achieve better device performance. Many recent studies have focused on the investigation of the mechanisms responsible for the anode degradation, such as Ni grain growth by sintering, carbon coking, sulfur poisoning and redox cycling [42,43]. In addition, different anode compositions have been studied, modifying both, the metallic phase, through metal substitution and, the support, employing samarium and gadolinium cermets, in order to avoid degradation, decrease of the operation temperature, increase of the cell performance and extend the type of fuel that can be used [44–58].

Another strategy investigate the possibility to avoid metal impregnation in the anodes, by synthesizing mixed ionic and electronic conductors (MIEC) perovskites, such as lanthanum strontium chromium manganites/ferrites, sintered at high temperatures (> 1000 °C) [40,43,59]. However, these anodes do not present high catalytic activity for methane oxidation; neither high electronic conductivity nor stability, therefore, the development of novel compositions or combinations of material structures is still an open area for research, motivated by the use of natural gas fuels [43].

The aim of this work was to synthesize and characterize ZDC with 90 mol% CeO_2, using a polymeric template route and two different calcination temperatures, in order to obtain porous ceramics, preferentially with a single crystalline phase. The ceramics impregnated with NiO were analyzed to evaluate their applicability in catalysis and as anodes of intermediate temperature solid oxide fuel cells (IT-SOFCs).

2. Materials and methods

2.1. Sample preparation

The ZDC synthesis used 0.5 g of Pluronic P-123 (BASF) for 5 mmol of Ce/Zr (molar ratio of 9/1). The polymer was previously stirred with 10.7 mL of 2 mol L^{-1} HCl solution before the addition of $CeCl_3{\cdot}7H_2O$ (Aldrich) and $ZrCl_4$ (Aldrich). The gel was stirred for 2 h and its pH was adjusted to 3 by adding concentrated NH_4OH. The hydrothermal treatment of the resulting mixture was performed in a Teflon autoclave for 48 h at 80 °C. The sample was dried at 60 °C for 1 day.

Calcination process at 400 °C was performed in a tubular oven, with a temperature heating rate of 1 °C min^{-1}, with an isotherm of 4 h at 400 °C, in air (sample named Z90C-c400). The other calcination used the same heating rate, until 540 °C in N_2 atmosphere, an isotherm at 540 °C with 2 h in N_2 and 2 h in air (sample named Z90C-c540). This last process was previously established for calcined ordered mesoporous silica [60].

The NiO was incorporated by incipient wetness impregnation (IWI) of $Ni(NO_3)_2{\cdot}6H_2O$ solution with anhydrous ethanol (99.99% purity). The solution with nickel nitrate and the ZDC solid was mixed in a proportion to obtain 60 (w/w)% of NiO after calcination. The impregnated solid was dried in an oven for 4 h and calcined until 350 °C with a heating rate of 1 °C min^{-1} and maintained at this temperature for 4 h.

2.2. ZDC and Ni/ZDC characterization

The X-ray diffraction measurements were performed with a Bruker D8 Discover-DaVinci equipment with a copper tube (Cu Kα radiation, λ=1.5418 Å), Ni filter and a Lynx-eye detector, operating at 40 kV and 30 mA, with 2θ from 20° to 100°, a 0.02° step and counting time of 10 s/step. The Rietveld's powder structure refinement analysis was performed using Fullprof software [61]. The peak shape was assumed as an asymmetric pseudo-Voigt function. The background of each pattern was fitted by a polynomial function (degree 5). The least-square method was adopted to minimize the difference between the observed and the simulated powder diffraction patterns.

Nitrogen adsorption isotherms (NAI) were obtained with an ASAP 2020 Micromeritics porosimeter. Thermal treatment was made during 12 h at 200 °C and the measurements were taken at 77 K (N_2). The pore size distribution (PSD), pore volume and pore diameter were calculated using the BJH (Barrett-Joyner-Halenda) method [62]. The specific surface area was calculated using the BET (Brunauer–Emmett–Teller) method [63]. Scanning electron microscopy (SEM) images were obtained with a field emission electron microscope JEOL JSM-7401F with 5.0–10.0 kV of acceleration tension, SEI secondary electron detector, working distance ranging from 2.0 to 6.0 mm and 1.0 nm resolution. Transmission electron microscopy (TEM) images and Energy Dispersive X-ray Spectroscopy (EDS) maps were collected at a JEOL model JEM-2100 with 50 kV of acceleration tension, resolution of 0.25 nm and sample inclination of ± 30°.

The small angle X-ray scattering (SAXS) measurements were carried out with a Bruker NANOSTAR sealed Cu tube (Cu Kα radiation, λ=1.5418 Å) operating at 40 kV and 30 mA, with a multi-filament Hi-STAR two-dimensional detector. The point focus geometry was used; the system was collimated by 3 pinholes and a cross-coupled Goebel-mirror system. The set up holds a vacuum path between the sample chamber and the detector. The sample to detector distance was 650 mm, therefore with q values ranging from 0.012 $Å^{-1}$ to 0.35 $Å^{-1}$. All the data were normalized by the measuring time and were corrected for the absorption effects. The inverse Fourier transform (IFT) method was used to perform the particle size distribution function in order to evaluate the porous structure of the samples, using the PCG software [64].

Temperature-programmed Reduction (TPR) was performed with a Micromeritics Chemisorb 2720. The samples were placed in a quartz reactor and prepared by heating in a He gas flow (50 mL min^{-1} at STP) until 300 °C for 1 h to eliminate water and other impurities. After the samples were cooled down to room temperature, then they were heated with a 10 °C min^{-1} ramp with 50 mL min^{-1} at STP gas flow mixture with 5 mol% H_2 in Ar balance. The thermocouple was placed inside the reactor, just above the catalyst bed, in order to avoid heat transfer limitations. H_2 consumption was monitored by the change in the thermal conductivity of the reactor exit gas flow with a thermal conductivity detector (TCD). The catalytic test for total methane oxidation was carried out in fixed-bed quartz tubular reactor with internal 10 mm diameter containing 50 mg of catalyst samples without any pretreatment. It was used a feed gas flow of 333 cm^3 min^{-1} at STP, consisted of CH_4 2 mol%, O_2 4 mol% and N_2 balance. Composition of feed and exhaust reactor gas flows were determined by on-line gas chromatography. A Clarus 500 (Perkin Elmer) equipped with a thermal conductivity detector and automatic injection valve was used. The reaction temperature was monitored by a thermocouple placed in the middle of the catalyst bed. Methane and oxygen conversions and carbon dioxide production were calculated according to the following expressions:

$$X_{CH4} = \frac{(F^i_{CH4} - F^o_{CH4})}{F^i_{CH4}} 100\% \quad (1)$$

$$X_{O2} = \frac{(F^i_{O2} - F^o_{O2})}{F^i_{O2}} 100\% \quad (2)$$

F^i_{CH4} and F^i_{O2} are the methane and oxygen molar flow in the feed, and F^o_{CH4} and F^o_{O2} are the molar flow in the exit. The CO_2 production is:

$$P_{CO2} = \frac{F^p_{CO2}}{F^i_{CH4}} 100\% \quad (3)$$

F^p_{CO2} corresponds to the molar flow of CO_2 in the exit.

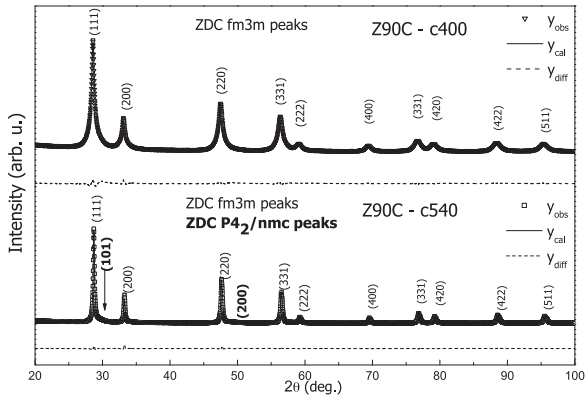

Fig. 1. Conventional XRD patterns for sample Z90C calcined at 400 and 540 °C (empty symbols) with the Rietveld fitted pattern (line) and the difference plot (dashed line).

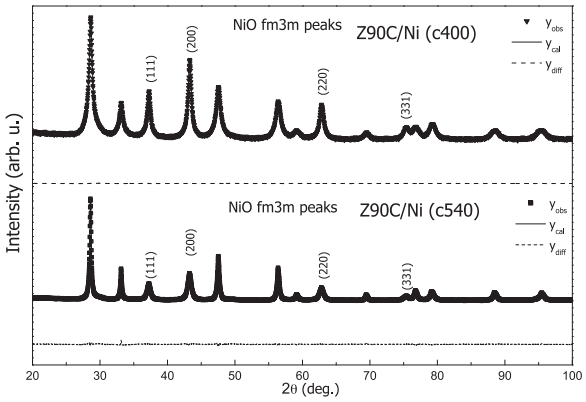

Fig. 2. Conventional XRD patterns for sample Z90C calcined at 400 and 540 °C after NiO impregnation (full symbols) with the Rietveld fitted pattern (line) and the difference plot (dashed line).

3. Results

3.1. X-ray diffraction and Rietveld analysis

X-ray diffractograms are presented in Fig. 1 and the Rietveld refinement results are shown in Table 1. The Rietveld refinement of the sample calcined at 400 °C resulted in a single cubic fluorite type $Fm\bar{3}m$ crystal structure (within the limits of the technique, which does not detect nanocrystalline phases with concentration lower than 3–4%). The Rietveld refinement of the sample calcined at 540 °C revealed the presence of a small concentration (~5%) of the zirconia-ceria tetragonal phase ($P4_2/nmc$). Raman spectroscopy could give a more precise determination of the crystalline phases in those samples [29,65]. The sample Z90C-c540, calcined in higher temperature, showed a larger average crystallite size than the sample heated until 400 °C (Z90C-c400). The sample Z90C-c540 was stable after heated until 1000 °C for more than 5 h. After this process the phase quantities were constant and there was only an increase in crystallite size. Also, the method produced samples with reproducible tetragonal phase content. The X-ray diffractograms after NiO impregnation are shown in Fig. 2 and the Rietveld results are shown in Table 2. The corresponding NiO peaks are present for both samples. As expected the ZDC structure was unaltered after NiO impregnation and the average crystallite size of NiO is almost the same for both calcination processes. The NiO weight fraction, obtained from the Rietveld refinement, is close to 60 w/w%, in good accordance with the nominal concentration.

Table 1
Structural parameters of Rietveld analysis for 90% CeO_2 calcined samples until 400 and 540 °C. The values of a and c are the lattice parameters, % of crystalline phases, V is the lattice volume, D is the average crystallite size. R_p, R_{wp}, R_{exp}, S_{GoF} and χ^2 are the Rietveld standard agreement factors.

Z90C-c400		Z90C-c540	
Phase	Cubic	Cubic	Tetragonal
	Fm3m	*Fm3m*	*P42/nmc*
	100%[a]	95.14%	4.86%
a/Å	5.4771(6)	5.4109(7)	3.731(2)
c/Å	–	–	5.148(5)
V/Å^3	158.97(3)	158.423(9)	71.66(9)
D/nm	16.8(2)	54(1)	3.2(7)
R_P	6.3	6.4	
R_{wp}	6.9	6.8	
R_{exp}	4.6	4.3	
S_{GoF}	1.5	1.6	
χ^2	2.3	2.5	

[a] Uncertainty of single phase between 3% and 4%.

Table 2
Structural parameters of Rietveld analysis for 90% CeO_2 calcined samples until 400 and 540 °C after NiO impregnation. The values of a and c are the lattice parameters, % of crystalline phases, V is the lattice volume, D is the average crystallite size. R_p, R_{wp}, R_{exp}, S_{GoF} and χ^2 are the Rietveld standard agreement factors.

Ni/Z90C (c400)			Ni/Z90C (c540)		
Phase	Cubic	NiO	Cubic	Tetragonal	NiO
	Fm3m	*Fm3m*	*Fm3m*	*P42/nmc*	*Fm3m*
	37.95%	62.05%	38.29%	2.29%	59.43%
a/Å	5.4156(14)	4.1878(12)	5.4115(10)	3.744(4)	4.1875(8)
c/Å	–	–	–	5.131(2)	–
V/Å^3	158.481(4)	73.214(20)	158.412(5)	71.92(2)	73.21(5)
D/nm	16.3(2)	20.2(3)	48(2)	4.6(1)	21.9(5)
R_P	8.9		9.7		
R_{wp}	7.2		7.1		
R_{exp}	5.9		5.3		
S_{GoF}	1.2		1.3		
χ^2	1.5		1.8		

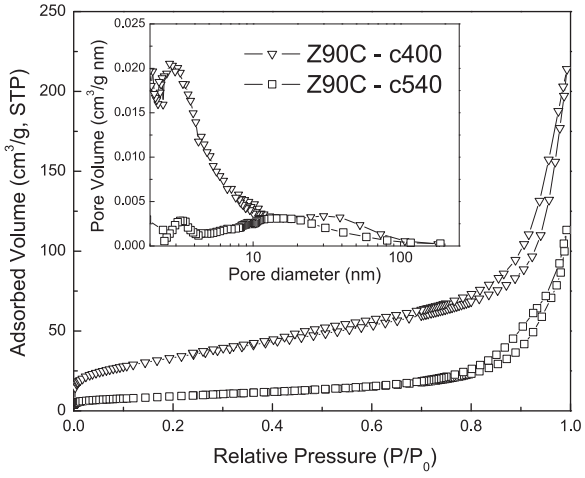

Fig. 3. Nitrogen physisorption isotherm and the pore size distribution (PSD) calculated from the adsorption branch using the BJH method for Z90C calcined until 400 and 540 °C.

3.2. Nitrogen isotherms and textural properties

Nitrogen physisorption results of Z90C samples, calcined at 400 °C and 500 °C, are shown in Fig. 3. Both samples presented an isotherm of type IV according to the IUPAC classification [66] with a low slope in the micropore region and did not show saturation at P/P_o~1, which can be attributed to large pores and inter-particle porosity. The Z90C-c400 sample showed an H_2-type hysteresis loop, characteristic of homo-

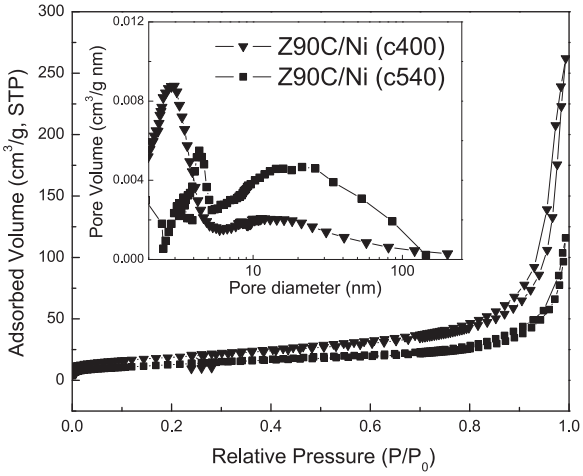

Fig. 4. Nitrogen physisorption isotherm and the pore size distribution (PSD) calculated from the adsorption branch using the BJH method for Z90C calcined until 400 and 540 °C after NiO impregnation.

geneous pore size and narrow particle size distributions. While Z90C-c540 sample showed an H_3-type hysteresis loop, which corresponds to small slit-like pores and a wide pore size distribution (PSD). During calcination these systems pass from an amorphous phase to crystalline oxides [66] and this process generates larger pores, as shown by the PSD behavior depicted in Fig. 3.

The isotherms after NiO impregnation are shown in Fig. 4. Table 3 presents the textural properties of all samples. Micropore volume and surface area were obtained through the t-plot method with the Harkins and Jura correction [67].

After the NiO impregnation both samples presented similar physisorption graphs, showing parallel isotherms to the relative pressure axis, suggesting the presence of small pores, since the adsorbed volume is almost constant for small P/P_o values. The best textural properties were obtained for the Z90C-c400 sample. After the NiO impregnation the BET and microporous surface area of the Z90C-c540 sample increased due to the porosity between the NiO particles over the ZDC matrix, confirmed by electron microscopy images.

3.3. SEM/TEM micrographs

The morphology of the samples was evaluated with scanning and transmission electron microscopy images. SEM micrographs (Fig. 5(a) and (b)) showed smaller particles for the ZDC samples calcined at 400 °C, before and after NiO impregnation, as expected since higher temperature tends to increase particle size. TEM images for Z90C-c540 showed the ZDC nanocrystals before (Fig. 6(a)) and after (Fig. 6(b)) NiO impregnation. The SEM and TEM images allowed visualizing the porous structure of the zirconia-ceria. The particle sizes varied from 26 to 96 nm. The TEM images showed a bicontinuous crystalline structure, mostly with cubic shape, with randomly distributed pores, having different sizes, smaller than 5 nm up to 50 nm. After the NiO impregnation the particle shape became round and the material looked like denser, with clusters ranging from 17 nm up to 214 nm. The energy dispersive X-ray spectroscopy (EDS) analysis (Supporting information) revealed a homogeneous distribution of Ni on top of the zirconia-ceria matrix and some small Ni particles (~3 nm) on the boundary region of the clusters. After NiO impregnation the pore sizes were between 5 nm and 22 nm.

Table 3
Nitrogen physisorption results: specific surface area S_{BET}, micropore surface area from t-plot method S_μ, pore volume V_P, micropore pore volume from t-plot method V_μ and mean pore diameter D_P, for ZrO_2-CeO_2 samples.

Samples	S_{BET} ($m^2\ g^{-1}$)	S_μ ($m^2\ g^{-1}$)	V_P ($cm^3\ g^{-1}$)	V_μ ($cm^3\ g^{-1}$)	D_P (nm)
Z90C-c400	119.9	30.0	0.40	0.016	3.3
Z90C-c540	32.1	1.64	0.18	0.001	10.7
Ni/Z90C(c400)	66.7	11.7	0.42	0.006	2.8/12
Ni/Z90C(c540)	43.3	19.4	0.21	0.011	4.3/19.1

3.4. SAXS results and modelling

SAXS results for Z90C-c400/-c540 are shown in Fig. 7. SAXS is a very powerful technique to evaluate general porous systems. It is a non-destructive method, which do not depend on molecule adsorption such as BET/BJH methods, so it can detect a wide range of pores. Since the samples do not have a very narrow pore size distribution shown by NAI results, the Inverse Fourier Transform (IFT) method [68] was used to evaluate the volume distribution of the pores ($D_V(R)$, Fig. 7(a)) and the distribution of the number of pores ($D_N(R)$, Fig. 7(b)), as a function of the pore dimension. The SAXS curves presented in Fig. 7(c) shows a typical porous bicontinuous biphasic system for both calcination temperatures.

The pore volume distribution $D_V(R)$ is in accordance with the adsorption results, the Z90C-c540 sample contains larger pores and a wider distribution compared to the Z90C-c400 sample. This agreement between these two independent data can also be confirmed by the higher scattering of Z90C-c540 sample in the low angle region in Fig. 7(c). Also, the $D_N(R)$ showed that lower the calcination temperature resulted in smaller pores.

The SAXS data after NiO impregnation, shown in Fig. 8, have a different outcome from the IFT calculations compared to Fig. 7. The SAXS curves, $D_V(R)$ and $D_N(R)$ have similar characteristics, which can be assigned as the NiO particles on the ZDC matrix. This can also explain why the PSD (Fig. 4, inset) also presented a peak in the smaller pore diameter range. Also, it can explain the isotherm behavior at lower relative pressure, once the Ni precursor can block part of the micropores, part of the mesopores and generate some porosity between particles after the heating treatment to form NiO.

3.5. TPR analysis

Temperature-programmed reduction profiles of the calcined samples and a ceria standard (LSA-CeO_2), with low specific surface area, are presented in Fig. 9. High superficial area ceria-based materials present low temperature peaks on the TPR profile because the reduction process is limited by its textural properties. In Fig. 9 it is possible to observe that the Z90C-c400 sample with higher superficial area presents a reduction behavior at lower temperatures, the reduction starts at 400 °C. These first peaks (430 and 530 °C) correspond to the superficial Ce^{4+} to Ce^{3+} reduction, while the high temperature peak (740 °C) is related to the bulk ions. In order to rule out the presence of impurities from the synthesis procedure in the sample calcined at 400 °C a thermal treatment was performed at 500 °C during 30 min in diluted O_2 (5 mol% O_2/He) prior to the TPR experiment. The TPR profile obtained (not presented here) exhibits the same two low temperature features at ca. 425 °C and 530 °C confirming that they correspond to the reduction of ceria. It can also be seen that the Z90C-c540 has a higher final reduction percentage when compared with the sample calcined at lower temperature. This could be related to the fact that this sample has higher pore diameters which could have facilitated the higher reduction. LSA-CeO_2 standard presents a peak at higher temperature (888 °C) indicating the strong influence of grain size and porosity on the reduction process. Both samples reached around 30% reduction at lower temperatures than the LSA-CeO_2 standard. The peak temperatures and hydrogen consumption are presented on Table 4.

The TPR profiles after NiO impregnation are shown on Fig. 10 with a LSA-NiO standard. The LSA-NiO standard TPR profile has one peak

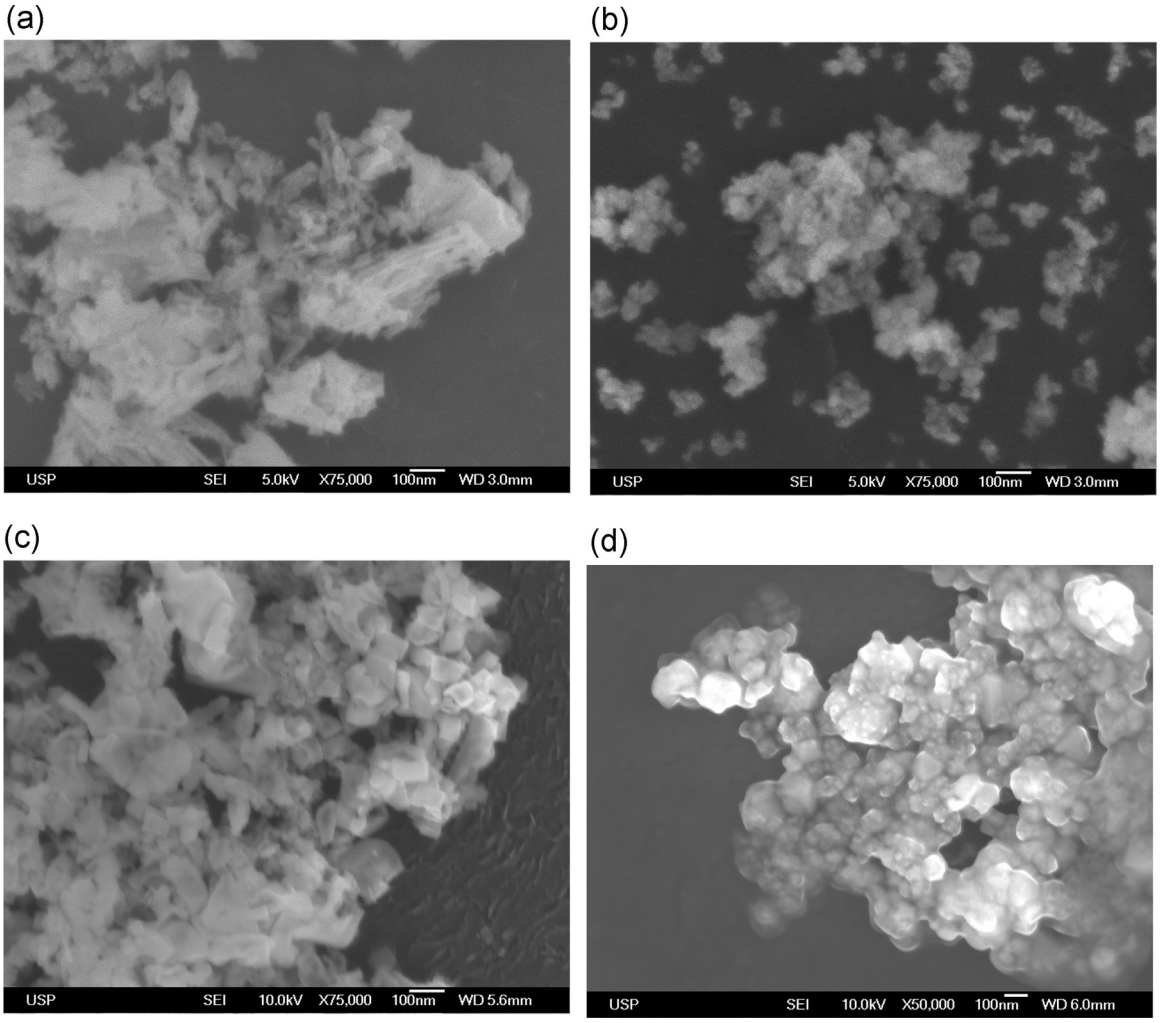

Fig. 5. Scanning electron microscopy images of Z90C samples: (a) Z90C-c400, (b) Ni/Z90C-c400, (c) Z90C-c540, (d) Ni/Z90C-c540.

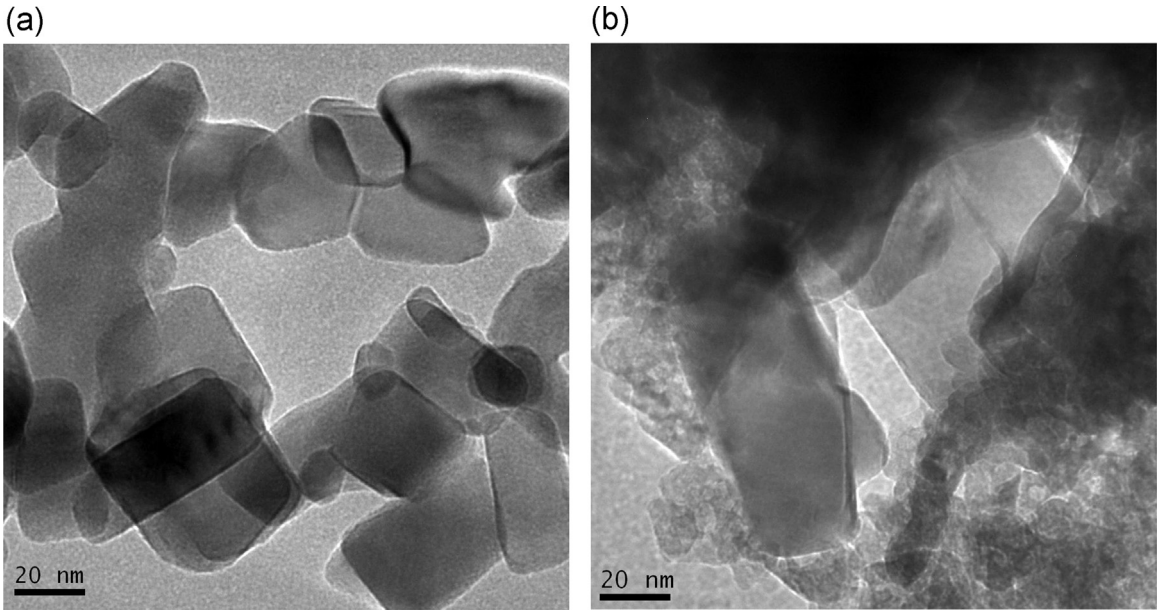

Fig. 6. Transmission electron microscopy images of Z90C samples: (a) Z90C-c540, (b) Ni/Z90C-c540.

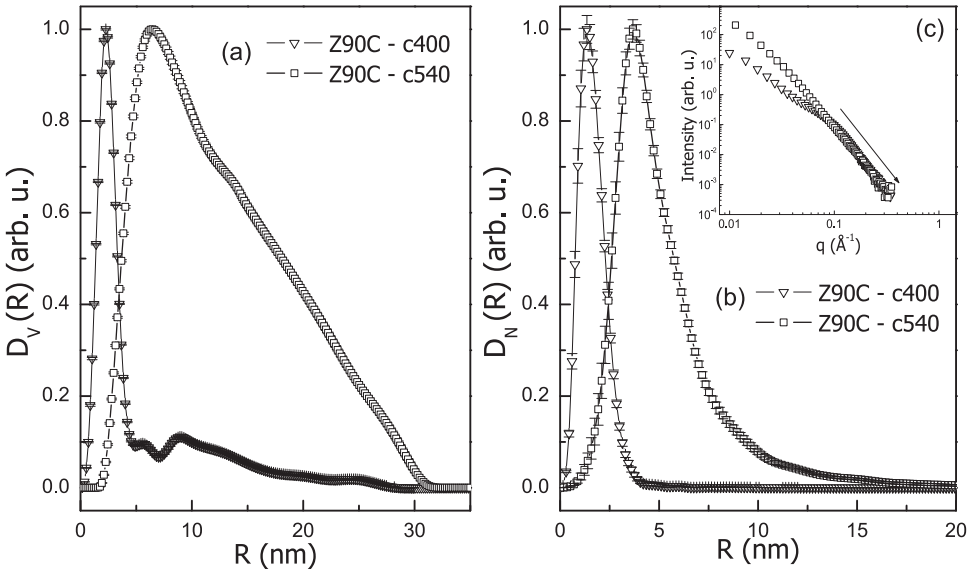

Fig. 7. (a) Volume (D_V(R)) and (b) number distribution (D_N(R)) and (c) SAXS curves for Z90C-c400 and Z90C-540.

around 400 °C and another one around 610 °C, which corresponds to the process controlled by diffusion inside large particles. The NiO-supported samples presented lower reduction temperature and an one-step reduction profile due to the distribution of this oxide on the high specific surface of the support, facilitating the diffusion process. Higher temperature peaks (see inset in Fig. 10) are overlapped with the post ZDC reduction. There was no 100% reduction of all Ce and Ni moles at lower temperatures, but evaluating the first peak and only taking into account the NiO in the samples, there was 100% NiO to Ni reduction for both samples around 400 °C.

3.6. Methane conversion

Catalytic activity test results are presented in Fig. 11. In Fig. 11(a) and (b) oxygen and methane conversion are plotted against temperature for samples Z90C/Ni(c400) and Z90C/Ni(c540). Both samples exhibit an increase in oxygen and methane conversion with an onset temperature for methane combustion reaction at ca. 450 °C. The only product detected was CO_2 with no traces of CO or H_2, indicating that in the analyzed temperature range only the complete oxidation of methane takes place. It should be noted that the oxygen conversion reaches 70% at 650 °C for both samples and a temperature for 50% conversion (T50) was attained at 550 °C, indicating an excellent catalytic activity for methane combustion at low temperatures. Similar catalysts presented T50 above 600–700 °C [36,37,69–72]. However, it is interesting to point out the differences between the O_2 and CH_4 conversion profiles of both catalysts. In the case of sample Z90C/Ni(c400) both O_2 and CH_4 conversion profiles match in the whole temperature range, whereas in the case of Z90C/Ni(c540), CH_4 conversion is higher than O_2 conversion, especially in the temperature range of 550–650 °C. This, altogether with the fact that CH_4 conversion is higher than CO_2 production (Fig. 11(c)), indicate that carbon formation might be taking place on the surface of the Z90C/Ni(c540) sample. In fact, carbon balance between inlet and exit from the reactor matched 100 ± 15% for the Z90C/Ni(c540) sample, whereas the Z90C/Ni(c400) sample exhibited a carbon balance that matched 100 ± 2% in all cases.

Catalyst characterization results presented in the previous sections

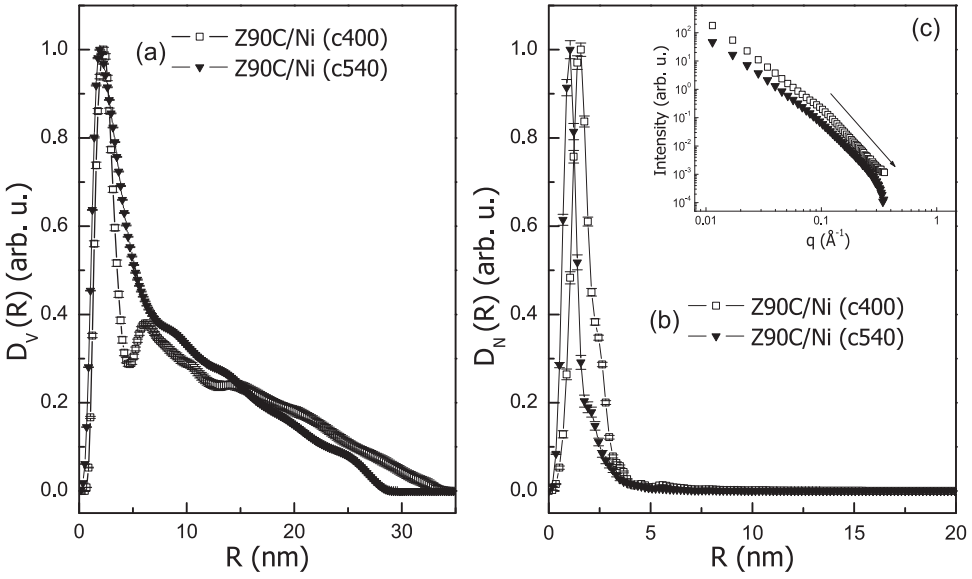

Fig. 8. (a) Volume (DV (R)) and (b) number distribution (D_N(R)) and (c) SAXS curves for Z90C/Ni (c400) and Z90C/Ni (c540).

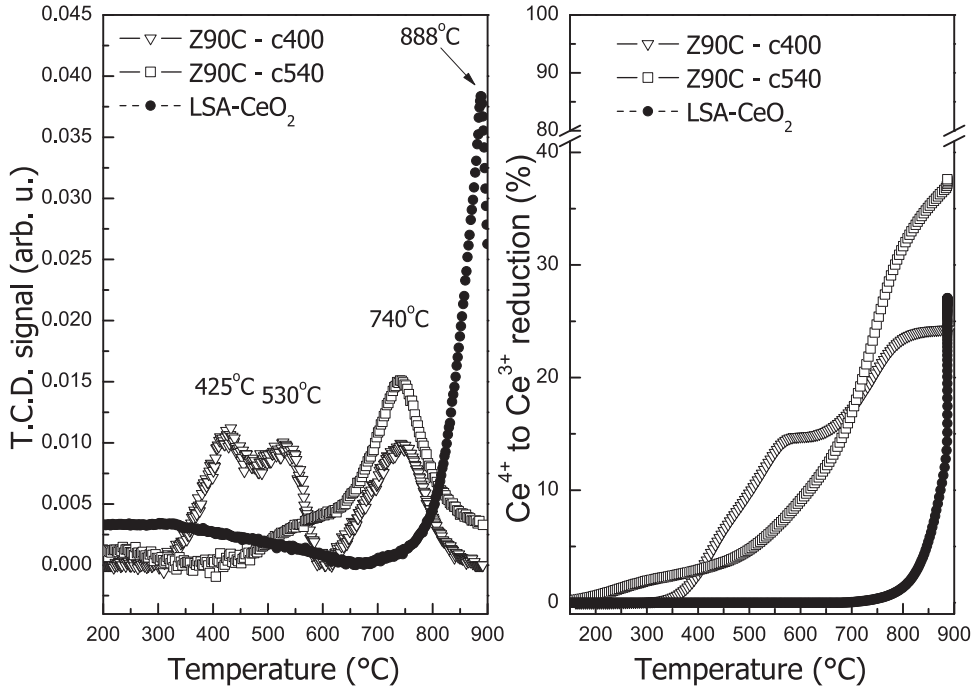

Fig. 9. Left: TPR profile Z90C for both calcination temperatures and LSA-CeO_2 standard. Right: Ce^{4+} to Ce^{3+} reduction with temperature.

Table 4
TPR results: hydrogen consumption at 25 °C and 1 atm (C_{H2}), temperature of the profile peaks (T_{Pi}, i=1,2,3, 1=first peak) and R is the total reduction of the Z90C/Ni samples.

Samples	C_{H2} (mL g^{-1})	T_{P1} (°C)	T_{P2} (°C)	T_{P3} (°C)	R (%)
Z90C-c400	16.0	–	425/530	740	25.3
Z90C-c540	25.4	–	552.7	740	37.6
LSA-CeO_2	19.2	888	–	–	27.1
Ni/Z90C(c400)	223.4	317.5	–	609.7	100
Ni/Z90C(c540)	175.3	322.2	515.0	686.9	78.8
LSA-NiO	314.1	404.5	590.8	–	96.0

revealed that as a result of the low temperature synthesis procedure and calcination temperature, the sample that was calcined at 400 °C exhibited a larger total pore volume, higher surface area and smaller crystallite sizes than the sample calcined at 540 °C. The morphological and textural properties led to an enhancement in NiO and CeO_2 reducibility in the case of Z90C/Ni(c400) sample. This enhancement in the ceria redox behavior might be responsible for an improved oxygen surface exchange allowing for gasification of carbon species in the sample fired at lower temperature [73].

4. Discussion

Porous anodes are more suitable to achieve low temperature operation of SOFCs, because they enhance the mass flow of gases that

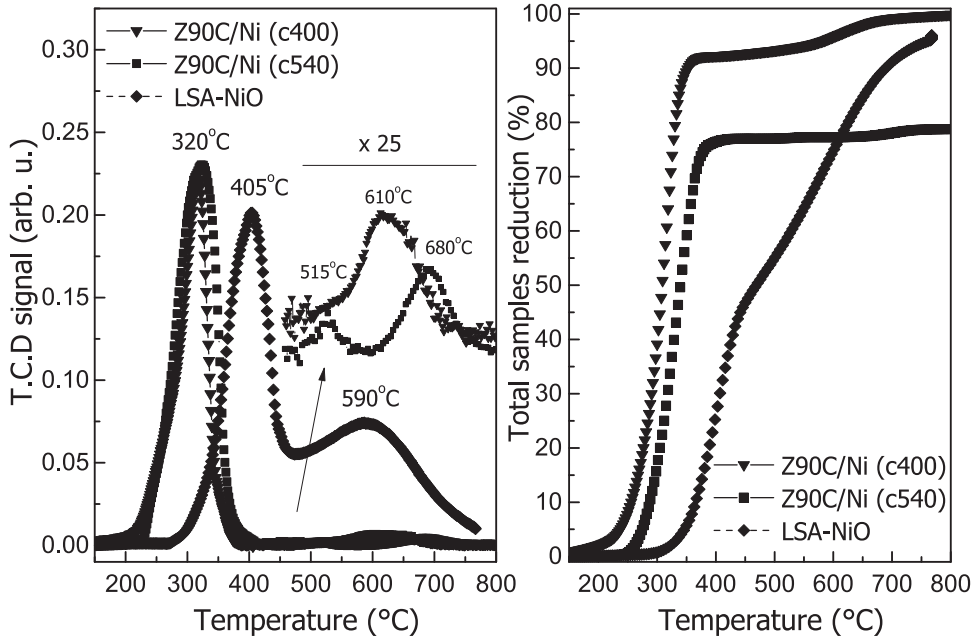

Fig. 10. Left: TPR profile Z90C/Ni for both calcination temperatures and LSA-NiO standard. Right: total (Ce^{4+} to Ce^{3+}+ Ni^{2+} to Ni^0) reduction with temperature.

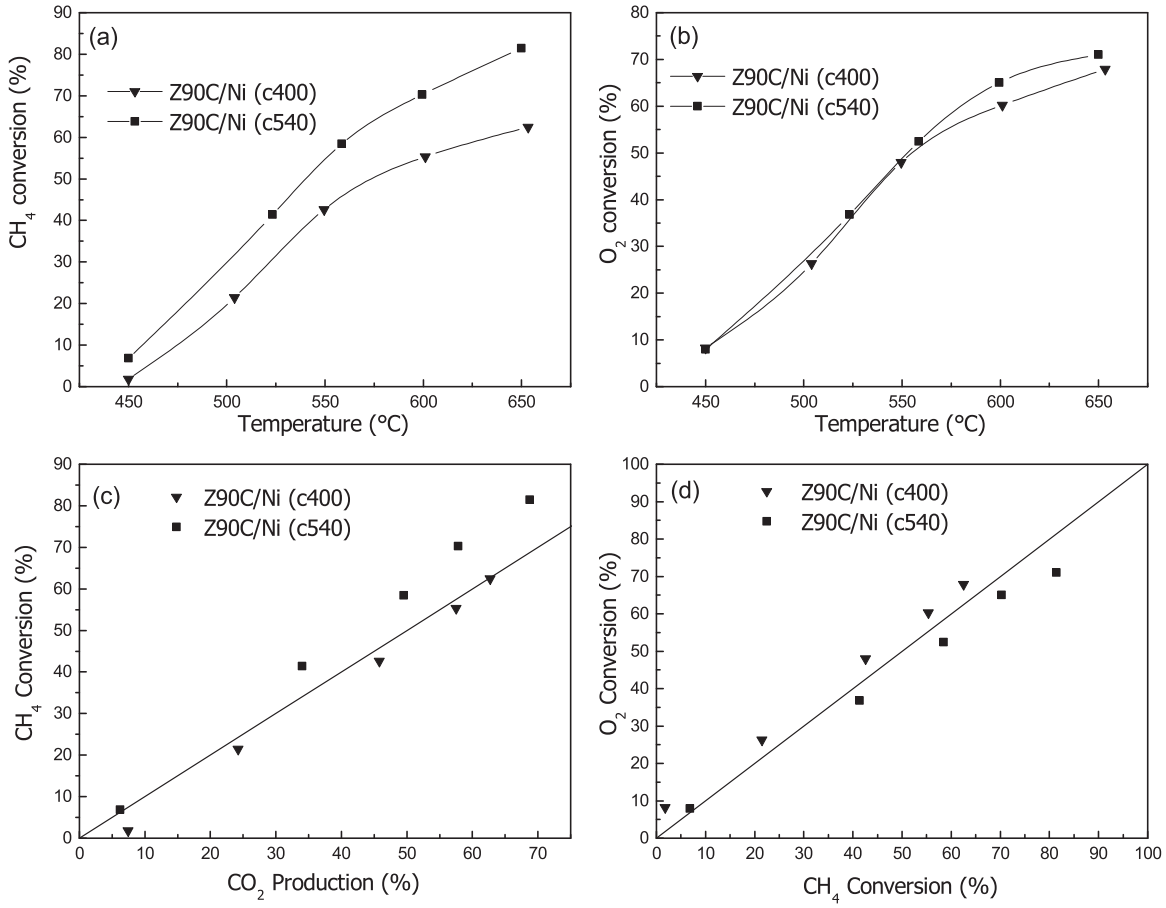

Fig. 11. Total methane conversion: (a) CH_4 conversion with temperature; (b) O_2 conversion with temperature, (c) CH_4 conversion as a function of CO_2 production, (d) Correlation between O_2 and CH_4 conversion; the lines in (c) and (d) represent a 45° line.

promotes the redox reactions, as well as the porosity improves the catalytic processes [68,74–76]. The properties of porous zirconia and ceria oxides are strongly dependent on the template and synthesis routes. Independent on the synthesis and template utilized, the initially ordered mesophase induced by the directing structure agent is commonly lost after calcination [66,77,78].

Similar results for CH_4 conversion at intermediate temperatures (550–650 °C) were obtained for NiO/ZrO_2-CeO_2 samples, synthesized by the gel-combustion route, evidencing the importance to prepare nanocrystalline composites [11], as those of this work, with crystallite sizes of 17 and 54 nm, calcined at 400 and 540 °C, respectively. Besides, the larger surface areas and pore diameters, obtained by the template method, were accountable for the larger Ce and Ni redox rates.

TPR experiments showed a higher Ni reduction rate for the sample calcined at 400 °C, because its higher surface area allowed a more homogeneous/smooth coverage of Ni atoms, avoiding aggregation. The increase in the micropore surface area and pore volume of the sample calcined at 540 °C after nickel impregnation is another indication of clustering of the nickel oxide particles. On the other hand, probably due to the rupture of the ZrO_2-CeO_2 walls, the sample calcined at 540 °C presented larger pores, allowing a greater exposition of the Ce atoms, giving a larger Ce reduction rate, as revealed by the TPR data. The TPR results showed higher redox figures and lower temperatures of the porous samples compared to the low surface area standards, demonstrating the potential of these materials as catalyzer and anodes of IT-SOFC. Also, there was no evidence of carbonaceous deposits during methane conversion, attesting for the quality of the developed electrodes. Long cycling experiments have to be performed in order to guarantee the anodes integrity.

It is worth to mention that the sample calcined at 540 °C (Z90C-c540) presented a mixture of crystalline phases (~95% cubic and ~5% tetragonal), nonetheless its Ce reduction figures (rate and temperature) were better than the standard material (LSA-CeO_2), demonstrating that the single phase requirement is not necessary in real devices. Moreover, it is important to point out the crystalline phase stability of the Z90C-c540 sample up to 1000 °C.

5. Conclusions

In this research a novel low temperature synthesis of nanometric Ni/ZDC with suitable textural and structural properties for catalysis and anode of SOFC applications was developed. Different calcination processes were useful to control the crystal size and to promote phase stabilization.

The SAXS data allowed evaluating the porosity at a larger scale, presenting consistent results with other independent experimental techniques such as N_2 physisorption and electron microscopy. TPR/methane conversion showed the total reduction of NiO to Ni at lower temperatures and at a higher conversion rate when compared to other data in the literature, with no evidence of carbonaceous deposits.

The materials synthesized in this research proved to be more active for the total oxidation of methane at low temperatures compared with data reported for similar materials in the literature, indicating the important role of the morphology of the ZDC support on reducibility and catalytic performance of the samples. The sample calcined at 400 °C exhibited better morphological and textural properties leading to an enhancement in NiO and CeO_2 reducibility, which might be responsible for the improvement in the gasification of carbon species as observed in catalytic tests.

Acknowledgements

Dr. L. S. Soeira for the SEM images and Dr. L. Otubo for the TEM images. M.C.A. Fantini is a CNPq researcher. Thanks are due to CNPq and FAPESP, Brazil, and ANPCyT (Argentina) for the financial support. The Ph.D. scholarships granted to Rebeca Bacani by CNPq and by CONICET to Lucía M. Toscani is gratefully acknowledged.

Appendix A. Supporting information

Supplementary data associated with this article can be found in the online version at http://dx.doi.org/10.1016/j.ceramint.2017.03.101.

References

[1] D. Terribile, A. Trovarelli, J. Lorca, C. Leitenburg, G. Dolcetti, The synthesis and characterization of mesoporous high-surface area ceria prepared using a hybrid organic/inorganic route, J. Catal. 178 (1) (1998) 299–308. http://dx.doi.org/10.1006/jcat.1998.2152.

[2] P. Fornasiero, J. Kaspar, M. Graziani, On the rate determining step in the reduction of CeO_2-ZrO_2 mixed oxides, Appl. Catal. B: Environ. 22 (1999) L11–L14.

[3] D.M. Lyons, K.M. Ryan, M.A. Morris, Preparation of ordered mesoporous ceria with enhanced thermal stability, J. Mater. Chem. 12 (2002) 1207–1212. http://dx.doi.org/10.1039/B104677M.

[4] J. Kaspar, P. Fornasiero, Nanostructured materials for advanced automotive depollution catalysts, J. Solid State Chem. 171 (2003) 19–29.

[5] G.R. Rao, B.G. Mishra, Structural, redox and catalytic chemistry of ceria based materials, Bull. Catal. Soc. India 2 (2003) 122–134 (doi:10.1.1.501.2664).

[6] C. Deeprasertkul, R. Longloilert, T. Chaisuwan, S. Wongkasemjit, Impressive low reduction temperature of synthesized mesoporous ceria via nanocasting, Mater. Lett. 130 (2014) 218–222. http://dx.doi.org/10.1016/j.matlet.2014.05.124.

[7] J. Kaspar, P. Fornasiero, M. Graziani, Use of CeO_2-based oxides in the three-way catalysis, Catal. Today 50 (1999) 285–298.

[8] J. Kaspar, P. Fornasiero, G. Balducci, R.D. Monte, N. Hickey, V. Sergo, Effect of ZrO_2 content on textural and structural properties of CeO_2-ZrO_2 solid solutions made by citrate complexation route, Inorg. Chim. Acta 349 (2003) 217–226.

[9] C. Ho, J.C. Yu, X. Wang, S. Laib, Y. Qiub, Meso- and macro-porous Pd/$Ce_xZr_{1-x}O_2$ as novel oxidation catalysts, J. Mater. Chem. 15 (2005) 2193–2201. http://dx.doi.org/10.1039/B500902B.

[10] M. Rezaei, S.M. Alavi, S. Sahebdelfar, L. Xinmei, L. Qian, Z.F. Yan, CO_2-CH_4 reforming over nickel catalysts supported on mesoporous nanocrystalline zirconia with high surface area, Energy Fuels 21 (2) (2007) 581–589. http://dx.doi.org/10.1021/ef0606005.

[11] S. Larrondo, A. Kodjaian, I.O. Fábregas, M.G. Zimicz, D.G. Lamas, N.E.W. de Reca, N.E. Amadeo, Methane partial oxidation using Ni/$Ce_{0.9}Zr_{0.1}O_2$ catalysts, Int. J. Hydrogen Energy 33 (13) (2008) 3607–3613. http://dx.doi.org/10.1016/j.ijhydene.2008.04.025.

[12] B.M. Reddy, P. Bharali, Y.-H. Seo, E.A. Prasetyanto, S.-E. Park, Surfactant controlled and microwave-assisted synthesis of highly active $Ce_xZr_{1-x}O_2$ nano-oxides for co-oxidation, Catal. Lett. 126 (1–2) (2008) 125–133. http://dx.doi.org/10.1007/s10562-008-9591-5.

[13] W. Cai, Q. Zhong, W. Zhao, Y. Bu, Focus on the modified $Ce_xZr_{1-x}O_2$ with the rigid benzene-multi-carboxylate ligands and its catalysis in oxidation of NO, Appl. Catal. B: Environ. 158–159 (2014) 258–268. http://dx.doi.org/10.1016/j.apcatb.2014.04.022.

[14] Q. Tan, C. Du, Y. Sun, L. Du, G. Yin, Y. Gao, Nickel-doped ceria nanoparticles for promoting catalytic activity of Pt/C for ethanol electrooxidation, J. Power Sources 263 (2014) 310–314. http://dx.doi.org/10.1016/j.jpowsour.2014.04.062.

[15] S. Song, R.O. Fuentes, R.T. Baker, Nanoparticulate ceria-zirconia anode materials for intermediate temperature solid oxide fuel cells using hydrocarbon fuels, J. Mater. Chem. 20 (2010) 9760–9769. http://dx.doi.org/10.1039/C0JM01741H.

[16] M. Morales, M. Navarro, X. Capdevila, J. Roa, M. Segarra, Processing of graded anode-supported micro-tubular sofcs based on samaria-doped ceria via gel-casting and spray-coating, Ceram. Int. 38 (5) (2012) 3713–3722. http://dx.doi.org/10.1016/j.ceramint.2012.01.015.

[17] N. Jaiswal, S. Upadhyay, D. Kumar, O. Parkash, Ca^{2+} and Sr^{2+} co-doped ceria/carbonates nanocomposites for low temperature solid oxide fuel cells: composite effect, Ceram. Int. 41 (10, part B) (2015) 15162–15169. http://dx.doi.org/10.1016/j.ceramint.2015.08.089.

[18] D. Bucevac, A. Radojkovic, M. Miljkovic, B. Babic, B. Matovic, Effect of preparation route on the microstructure and electrical conductivity of co-doped ceria, Ceram. Int. 39 (4) (2013) 3603–3611. http://dx.doi.org/10.1016/j.ceramint.2012.10.188.

[19] M. Stojmenovic, S. Boskovi, M. Zunic, J. Varela, M. Prekajski, B. Matovic, S. Mentus, Electrical properties of multidoped ceria, Ceramics 40 (7) (2014) 9285–9292. http://dx.doi.org/10.1016/j.ceramint.2014.01.151.

[20] M.O. Mazan, J. Marrero-Jerez, A. Soldati, P. Nunez, S.A. Larrondo, Fe doped ceria nanopowders synthesized by freeze-drying precursor method for electrocatalytic applications, Int. J. Hydrogen Energy 40 (10) (2015) 3981–3989. http://dx.doi.org/10.1016/j.ijhydene.2015.01.006.

[21] Q. Huo, D.I. Margolese, P. Feng, T.E. Gier, G.D. Stucky, R. Leon, P.M. Petroff, U. Ciesla, F. Schuth, Generalized syntheses of periodic surfactant/inorganic composite materials, Nature 368 (1994) 317–321. http://dx.doi.org/10.1038/368317a0.

[22] A. Sayari, P. Liu, Non-silica periodic mesostructured materials: recent progress, Microporous Mesoporous Mater. 12 (4) (1997) 149–177. http://dx.doi.org/10.1016/S0927-6513(97)00059-X.

[23] P. Yang, D. Zhao, D.I. Margolese, B.F. Chmelka, G.D. Stucky, Generalized syntheses of large-pore mesoporous metal oxides with semicrystalline frameworks, Nature 396 (1998) 152. http://dx.doi.org/10.1038/24132.

[24] U. Ciesla, F. Schuth, Ordered mesoporous materials, Microporous Mesoporous Mater. 27 (2–3) (1999) 131–149. http://dx.doi.org/10.1016/S1387-1811(98)00249-2.

[25] P.D. Yang, D.Y. Zhao, D.I. Margolese, B.F. Chmelka, G.D. Stucky, Block copolymer templating syntheses of mesoporous metal oxides with large ordering lengths and semicrystalline framework, Chem. Mater. 11 (10) (1999) 2813–2826. http://dx.doi.org/10.1021/cm990185c.

[26] P. Fornasiero, G. Balducci, R.D. Monte, J. Kaspar, V. Sergo, G. Gubitosa, A. Ferrero, M. Graziani, Modification of the redox behavior of CeO_2 induced by structural doping with ZrO_2, J. Catal. 164 (1996) 173–183.

[27] G. Vlaic, R.D. Monte, P. Fornasiero, E. Fonda, J. Kaspar, M. Graziani, The CeO_2-ZrO_2 system: redox properties and structural relationships, Stud. Surf. Sci. Catal. 116 (1998) 185–195.

[28] D.G. Lamas, M.F. Bianchetti, M.D. Cabezas, N.E. Walsöe de Reca, Nanostructured ceramic materials: applications in gas sensors and solid-oxide fuel cells, J. Alloy. Compd. 495 (2010) 548–551. http://dx.doi.org/10.1016/j.jallcom.2009.10.014.

[29] D.G. Lamas, G.E. Lascalea, R.E. Juarez, E. Djurado, L. Perez, N.E.W. Reca, Metastable forms of the tetragonal phase in compositionally homogeneous, nanocrystalline zirconia-ceria powders synthesized by gel-combustion, J. Mater. Chem. 13 (4) (2003) 904–910. http://dx.doi.org/10.1039/b210500b.

[30] G.E. Lascalea, D.G. Lamas, L. Perez, E.D. Cabanillas, N.W. de Reca, Synthesis of ZrO_2-15 mol% CeO_2 nanopowders by a pH-controlled nitrate – glycine process, Mater. Lett. 58 (20) (2004) 2456–2460. http://dx.doi.org/10.1016/j.matlet.2004.02.036.

[31] D.G. Lamas, R.O. Fuentes, I.O. Fábregas, M.E.F. de Rapp, G.E. Lascalea, J.R. Casanova, N.E.W. de Reca, A.F. Craievich, Synchrotron X-ray diffraction study of the tetragonal-cubic phase boundary of nanocrystalline ZrO_2-CeO_2 synthesized by a gel-combustion process, J. Appl. Crystallogr. 38 (2005) 867–873. http://dx.doi.org/10.1107/S0021889805025343.

[32] I. Fabregas, R. Fuentes, D. Lamas, M.F. de Rapp, N.W. de Reca, M.C.A. Fantini, A. Craievich, R. Millen, M. Temperini, Local structure of the metaloxygen bond in compositionally homogeneous, nanocrystalline ZrO_2-CeO_2 solid solutions synthesized by a gel-combustion process, J. Phys.: Condens. Matter 18 (34) (2006) 7863–7881. http://dx.doi.org/10.1088/0953-8984/18/34/002.

[33] L.M. Acuna, F.F. Munoz, M.D. Cabezas, D.G. Lamas, A.G. Leyva, M.C.A. Fantini, R.T. Baker, R.O. Fuentes, Improvement in the reduction behavior of novel ZrO_2-CeO_2 solid solutions with a tubular nanostructure by incorporation of Pd, J. Phys. Chem. C 114 (46) (2010) 19687–19696. http://dx.doi.org/10.1021/jp108429t.

[34] M. Zimicz, S.A. Larrondo, R.J. Prado, D.G. Lamas, Time-resolved in situ XANES study of the redox properties of $Ce_{0.9}Zr_{0.1}O_2$ mixed oxides, Int. J. Hydrogen Energy 37 (2012) 14881–14886. http://dx.doi.org/10.1016/j.ijhydene.2012.01.162.

[35] L.M. Toscani, M.G. Zimicz, J.R. Casanova, S.A. Larrondo, NiCu/$Ce_{0.9}Zr_{0.1}O_2$ bimetallic cermets for electrochemical and catalytic applications, Int. J. Hydrogen Energy 39 (16) (2014) 8759–8766. http://dx.doi.org/10.1016/j.ijhydene.2013.12.035.

[36] M.G. Zimicz, B.A. Reznik, S.A. Larrondo, Conversion of biogas to synthesis gas over NiO/CeO_2-Sm_2O_3 catalysts, Fuel 149 (2015) 95–99. http://dx.doi.org/10.1016/j.fuel.2014.09.024.

[37] M.G. Zimicz, F.D. Prado, A.L. Soldati, D.G. Lamas, S.A. Larrondo, XPD and XANES studies of $Ce_{0.9}Zr_{0.1}O_2$ nanocatalysts under redox and catalytic CH_4 oxidation conditions, J. Phys. Chem. C 119 (33) (2015) 19210–19217. http://dx.doi.org/10.1021/acs.jpcc.5b05253.

[38] J. Marrero-Jereza, S. Larrondo, E. Rodriguez-Castellon, P. Nunez, TPR, XRD and XPS characterization of ceria-based materials synthesized by freeze drying precursor method, Ceram. Int. 40 (5) (2013) 6807–6814. http://dx.doi.org/10.1016/j.ceramint.2013.11.143.

[39] M. Lebreton, B. Delanoue, E. Baron, F. Ricoul, A. Kerihuel, A. Subrenat, O. Joubert, A. Le Gal La Salle, Effects of carbon monoxide, carbon dioxide, and methane on nickel/yttria-stabilized zirconia-based solid oxide fuel cells performance for direct coupling with a gasifier, Int. J. Hydrogen Energy 40 (2015) 10231–10241. http://dx.doi.org/10.1016/j.ijhydene.2015.06.009.

[40] S.Y. Gómez, D. Hotza, Current developments in reversible solid oxide fuel cells, Renew. Sustain. Energy Rev. 61 (2016) 155–174. http://dx.doi.org/10.1016/j.rser.2016.03.005.

[41] A. Lanzini, C. Guerra, P. Leone, M. Santarelli, F. Smeacetto, S. Fiorilli, A. Gondolini, E. Mercadelli, A. Sanson, N.P. Brandon, Influence of the microstructure on the catalytic properties of SOFC anodes under dry reforming of methane, Mater. Lett. 164 (2016) 312–315. http://dx.doi.org/10.1016/j.matlet.2015.10.171.

[42] M.S. Khan, S.-B. Lee, R.-H. Song, J.-W. Lee, T.-H. Lim, S.-J. Park, Fundamental mechanisms involved in the degradation of nickel–yttria stabilized zirconia (Ni–YSZ) anode during solid oxide fuel cells operation: a review, Ceram. Int. 42 (2016) 35–48. http://dx.doi.org/10.1016/j.ceramint.2015.09.006.

[43] T.M. Gür, Comprehensive review of methane conversion in solid oxide fuel cells: prospects for efficient electricity generation from natural gas, Prog. Energy Combust. Sci. 54 (2016) 1–64. http://dx.doi.org/10.1016/j.pecs.2015.10.004.

[44] M. Morales, F. Espiell, M. Segarra, Improvement of performance in low temperature solid oxide fuel cells operated on ethanol and air mixtures using Cu-ZnO-Al_2O_3

catalyst layer, J. Power Sources 293 (2015) 366–372. http://dx.doi.org/10.1016/j.jpowsour.2015.05.097.
[45] N.T.Q. Nguyen, T.A. Trieu, H.H. Yoon, Preparation of La/Co/Ni-based anode catalyst for biogas-fueled solid oxide fuel cells, J. Electroceram. 35 (2015) 75–80. http://dx.doi.org/10.1007/s10832-015-9994-9.
[46] K. Park, S. Lee, G. Bae, J. Bae, Performance analysis of Cu, Sn and Rh impregnated NiO/CGO91 anode for butane internal reforming SOFC at intermediate temperature, Renew. Energy 83 (2015) 483–490. http://dx.doi.org/10.1016/j.renene.2015.04.070.
[47] A.L. da Silva, N.C. Heck, Oxide incorporation into Ni-based solid oxide fuel cell anodes for enhanced sulfur tolerance during operation on hydrogen or biogas fuels: a comprehensive thermodynamic study, Int. J. Hydrogen Energy 40 (2015) 2334–2353. http://dx.doi.org/10.1016/j.ijhydene.2014.12.037.
[48] Ö. Yıldız, A.M. Soydan, M. Akel, E.F. Ipçizade, A. Ata, Characterization of Mo_y-M_x $Ce_{1-x}O_{2-\delta}$(M: Co, Ni & Cu) nano powders and anode materials for low and intermediate temperature solid oxide fuel cells, Int. J. Hydrogen Energy 40 (2015) 14085–14094. http://dx.doi.org/10.1016/j.ijhydene.2015.07.065.
[49] Y. Choi, E.C. Brown, S.M. Haile, W.C. Jung, Electrochemically modified, robust solid oxide fuel cell anode for direct hydrocarbon utilization, Nano Energy 23 (2016) 161–171. http://dx.doi.org/10.1016/j.nanoen.2016.03.015.
[50] R. Fernández-González, J.C. Ruiz-Morales, J. Canales-Vázquez, J.R. Jurado, Ahmed Makradi, Pedro Núñez, Decreasing the polarisation resistance of a Ni-YSZ solid oxide fuel cell anode by infiltration of a ceria based solution, Int. J. Hydrogen Energy 41 (2016) 19731–19736. http://dx.doi.org/10.1016/j.ijhydene.2016.03.092.
[51] Z. Jamil, E. Ruiz-Trejo, P. Boldrin, N.P. Brandon, Anode fabrication for solid oxide fuel cells: electroless and electrodeposition of nickel and silver into doped ceria scaffolds, Int. J. Hydrogen Energy 41 (2016) 9627–9637. http://dx.doi.org/10.1016/j.ijhydene.2016.04.061.
[52] J.G. Lee, O.S. Jeon, H.J. Hwang, J.J. Yeayeon Lee, S.H. Hyun, Y.G. Shul, Durable and high-performance direct-methane fuel cells with coke-tolerant ceria-coated Ni Catalysts at reduced temperatures, Electrochim. Acta 191 (2016) 677–686. http://dx.doi.org/10.1016/j.electacta.2016.01.091.
[53] A.F.S. Molouk, J. Yang, T. Okanishi, H. Muroyama, T. Matsui, K. Eguchi, Comparative study on ammonia oxidation over Ni based cermet anodes for solid oxide fuel cells, J. Power Sources 305 (2016) 72–79. http://dx.doi.org/10.1016/j.jpowsour.2015.11.085.
[54] D.A. Osinkina, N.M. Bogdanovich, A.L. Gavrilyuka, Rate determining steps of fuel oxidation over CeO_2 impregnated Ni-YSZ in H_2+H_2O+CO+CO_2 ambient, Electrochim. Acta 199 (2016) 108–115. http://dx.doi.org/10.1016/j.electacta.2016.03.133.
[55] J. Qu, W. Wang, Y. Chen, X. Deng, Z. Shao, Stable direct-methane solid oxide fuel cells with calcium-oxide-modified nickel-based anodes operating at reduced temperatures, Appl. Energy 164 (2016) 563–571. http://dx.doi.org/10.1016/j.apenergy.2015.12.014.
[56] V.A. Rojek-Wöckner, A.K. Opitz, M. Brandner, J. Mathé, M. Bram, A novel Ni/ceria-based anode for metal-supported solid oxide fuel cells, J. Power Sources 328 (2016) 65–74. http://dx.doi.org/10.1016/j.jpowsour.2016.07.075.
[57] K. Zhao, B.-H. Kim, Y. Du, Q. Xu, B.-G. Ahn, Ceria catalyst for inert-substrate-supported tubular solid oxide fuel cells running on methane fuel, J. Power Sources 314 (2016) 10–17. http://dx.doi.org/10.1016/j.jpowsour.2016.02.079.
[58] T. Montini, M. Melchionna, M. Monai, P. Fornasiero, Fundamentals and catalytic applications of CeO2-based materials, Chem. Rev. 116 (10) (2016) 5987–6041. http://dx.doi.org/10.1021/acs.chemrev.5b00603.
[59] M. Roushanafshar, N. Yan, K.T. Chuang, J.-L. Luo, Electrochemical oxidation of sour natural gas over $La_{0.4}Ce_{0.6}O_{1.8}$ –$La_{0.4}Sr_{0.6}TiO_{3\pm\delta}$ anode in SOFC: a mechanism study of H_2S effects, Appl. Catal. B: Environ. 176–177 (2015) 627–636. http://dx.doi.org/10.1016/j.apcatb.2015.04.046.
[60] J.R. Matos, L.P. Mercuri, M. Kruk, M. Jaroniec, Toward the synthesis of extra-large-pore MCM-41 analogues, Chem. Mater. 13 (5) (2001) 1726–1731. http://dx.doi.org/10.1021/cm000964p.
[61] J. Rodriguez-Carvajal, An introduction to the program Fullprof 2000, Laboratoire Leon Brillouin (CEA-CNRS), 2001.
[62] E.P. Barrett, L.G. Joyner, P.P. Halenda, The determination of pore volume and area distributions in porous substances. I. Computations from nitrogen isotherms, J. Am. Chem. Soc. 73 (1) (1951) 373–380. http://dx.doi.org/10.1021/ja01145a126.
[63] S. Brunauer, P.H. Emmett, E. Teller, Adsorption of gases in multimolecular layers, J. Am. Chem. Soc. 60 (2) (1938) 309–319. http://dx.doi.org/10.1021/ja01269a023.
[64] O. Glatter, A new method for the evaluation of small-angle scattering data, J. Appl. Cryst. 10 (1977) 415–421. http://dx.doi.org/10.1107/S0021889877013879.
[65] T. Montini, A. Speghini, L. De Rogatis, B. Lorenzut, M. Bettinelli, M. Graziani, A.P. Fornasiero, Identification of the structural phases of CexZr1-xO2 by Eu(III) luminescence studies, J. Am. Chem. Soc. 131 (2009) 13155–13160. http://dx.doi.org/10.1021/ja905158p CCC: $40.75.
[66] R. Bacani, T.S. Martins, M.C.A. Fantini, D.G. Lamas, Structural studies of mesoporous ZrO_2-CeO_2 and ZrO_2-CeO_2/SiO_2 mixed oxides for catalytical applications, J. Alloy. Compd. 671 (2016) 396–402. http://dx.doi.org/10.1016/j.jallcom.2016.01.213.
[67] W.D. Harkins, G. Jura, Surfaces of solids. XIII. A vapor adsorption method for the determination of the area of a solid without the assumption of a molecular area, and the areas occupied by nitrogen and other molecules on the surface of a solid, J. Am. Chem. Soc. 66 (8) (1944) 1366–1373.
[68] M.A. Morris, H.M. Reidy, Preparation of ceria–zirconia and yttria–zirconia mixed oxides of unusual pore structures, Ceram. Int. 31 (2005) 929–935. http://dx.doi.org/10.1016/j.ceramint.2004.10.006.
[69] W.-S. Dong, H.-S. Roh, K.-W. Jun, S.-E. Park, Y.-S. Oh, Methane reforming over Ni/Ce-ZrO2 catalysts: effect of nickel content, Appl. Catal. A: Gen. 226 (2002) 63–72.
[70] J. Chen, Q. Wu, J. Zhang, J. Zhang, Effect of preparation methods on structure and performance of Ni/$Ce_{0.75}Zr_{0.25}O_2$ catalysts for CH_4–CO_2 reforming, Fuel 87 (2008) 2901–2907.
[71] A. Larimi, S. Alavi, Ceria-zirconia supported Ni catalysts for partial oxidation of methane to synthesis gas, Fuel 102 (2012) 366–371.
[72] S. Xu, X. Wang, Highly active and coking resistant Ni/CeO_2–ZrO_2 catalyst for partial oxidation of methane, Fuel 84 (2005) 563–567.
[73] Z.-hua Gao, L.-feng Hao, W. Huang, K.-chang Xie, A novel liquid-phase technology for the preparation of slurry catalysts, J. Catal. Lett. 102 (3) (2005) 139–141. http://dx.doi.org/10.1007/s10562-005-5845-7.
[74] S. Somacescu, M. Florea, P. Osiceanu, J.M. Calderon-Moreno, C. Ghica, J.M. Serra, Ni-doped ($CeO_{2-\delta}$)–YSZ mesoarchitectured with nanocrystalline framework: the effect of thermal treatment on structure, surface chemistry and catalytic properties in the partial oxidation of methane (CPOM), J. Nanopart. Res. 17 (2015) 426–442. http://dx.doi.org/10.1007/s11051-015-3206-z.
[75] M.J. López-Robledo, M.A. Laguna-Bercero, J. Silva, V.M. Oreraa, A. Larrea, Electrochemical performance of intermediate temperature micro-tubular solid oxide fuel cells using porous ceria barrier layers, Ceram. Int. 41 (2015) 7651–7660. http://dx.doi.org/10.1016/j.ceramint.2015.02.093.
[76] Y. Zheng, X. Zhu, H. Wang, K. Li, Y. Wang, Y. Wei, Characteristic of macroporous CeO_2-ZrO_2 oxygen carrier for chemical-looping steam methane reforming, J. Rare Earths 32 (9) (2014) 842–848. http://dx.doi.org/10.1016/S1002-0721(14)60151-4.
[77] F. Kleitz, W. Schmidt, F. Schüth, Evolution of mesoporous materials during the calcination process: structural and chemical behavior, Microporous Mesoporous Mater. 44–45 (2001) 95–109.
[78] D. Gu, F. Schüth, Synthesis of non-siliceous mesoporous oxides, Chem. Soc. Rev. 43 (2014) 313–344. http://dx.doi.org/10.1039/c3cs60155b.